Improved modeling of the discrete component of the Galactic interstellar γ-ray emission and implications for the *Fermi*–LAT Galactic Center excess

Christopher M. Karwin [1,2,*] Alex Broughton [2,†] Simona Murgia [2,‡] Alexander Shmakov [3,§]
Mohammadamin Tavakoli [3,‖] and Pierre Baldi [3,¶]

[1] *Department of Physics and Astronomy, Clemson University, Clemson, South Carolina 29634, USA*
[2] *Department of Physics and Astronomy, University of California, Irvine, California 92697, USA*
[3] *Department of Computer Science, University of California, Irvine, California 92697, USA*

The aim of this work is to improve models for the γ-ray discrete or small-scale structure related to H_2 interstellar gas. Reliably identifying this contribution is important to disentangle γ-ray point sources from interstellar gas, and to better characterize extended γ-ray signals. Notably, the *Fermi*–LAT Galactic center (GC) excess, whose origin remains unclear, might be smooth or pointlike. If the data contain a pointlike contribution that is not adequately modeled, a smooth GC excess might be erroneously deemed to be pointlike. We improve models for the H_2-related γ-ray discrete emission for a $50° × 1°$ region along the Galactic plane via H_2 proxies better suited to trace these features. We find that these are likely to contribute significantly to the γ-ray *Fermi*–LAT data in this region, and the brightest ones are likely associated with detected *Fermi*–LAT sources, a compelling validation of this methodology. We discuss prospects to extend this methodology to other regions of the sky and implications for the characterization of the GC excess.

I. INTRODUCTION

The Galactic γ-ray interstellar emission (IE) traces interactions of cosmic rays (CRs) with the interstellar medium, and constitutes most of the γ-ray emission observed by *Fermi*–LAT. Uncertainties in modeling the IE are large and difficult to constrain, and they impact the study of other γ-ray sources in the *Fermi*–LAT data, pointlike as well as extended. We focus on modeling the small-scale structure of the IE which, if not robustly captured by the model, confuses the determination of point sources, especially along the Galactic plane [1]. It was shown in [2] that a large fraction of the point sources detected by *Fermi*–LAT in the Galactic center (GC) region could be misidentified gas structure, and strongly dependent in number and spatial distribution on the IE model employed to analyze the data. This result indicates the presence of pointlike emission in the data arising from unmodeled structure in the interstellar gas, and it underlines the importance of accurately modeling this component to reliably identify point sources in the γ-ray data. Also, evidence is found in the 4FGL-DR3 for clustering of

unassociated, spectrally soft sources along the Galactic plane that appears to be tracing interstellar clouds [3]. This emission could be originating from small-scale molecular gas structure.

More reliable modeling of the small scale gas structure could also impact the characterization of extended sources. A prominent example is the *Fermi*–LAT GC excess (see e.g. [2,4–13].) Striking features of this excess are its spatial morphology and spectrum which could be consistent with annihilating dark matter (DM). Alternative explanations have been proposed, with the leading one attributing the signal to a collection of discrete emitters such as an unresolved point source population of millisecond pulsars. Deviations from a spherically symmetric morphology for the excess have also been claimed which would imply the emission to be compatible with the stellar distribution in the Galactic bulge [14–17]. The origin of the *Fermi*-LAT GC excess remains a debated topic [18]. This debate could be settled by determining whether the spatial morphology of the excess is consistent with a smooth distribution, as predicted for DM, or with the cumulative emission of a collection of pointlike emitters. Statistical techniques have been employed to accomplish this [19–28], including the non-Poissonian template fit (NPTF) which can detect upward fluctuations in the photon statistics above Poisson noise which are associated with a collection of point sources. However, the results of the NPTF technique depend on the modeling of the IE (e.g. [21,23,24], but also [25,27]), and an uncontroversial resolution to the origin of

*ckarwin@clemson.edu
†abrought@uci.edu
‡smurgia@uci.edu
§ashmakov@uci.edu
‖mohamadt@uci.edu
¶pfbaldi@uci.edu

the GC excess has not yet been reached. We posit that if the interstellar gas is more structured and pointlike than current models predict, the unresolved point source contribution in the data could be erroneously inflated by the fainter component (also below detection threshold) of the small scale gas features. In particular, statistical methods such as the NPTF might attribute this component to a smooth GC excess and conclude it is pointlike. These uncertainties might therefore hinder the ability to distinguish the smooth versus pointlike duplicity of the excess. We note that wavelet decomposition is another statistical technique that has been employed to resolve the GC excess. While these studies are not as impacted by the IE model [19], the related results on the nature of the GC excess remain uncertain nonetheless [22,29].

II. MODELING THE INTERSTELLAR H_2 DISCRETE COMPONENT

In this work, we present a novel approach to improve modeling of the small-scale structure in the interstellar gas. The IE is due primarily to CRs interacting with the interstellar hydrogen gas (and radiation field), in molecular (H_2), atomic (HI), and ionized (HII) forms. The H_2 component is the most highly structured, and this structure is traced by the related γ-ray emission. In this work, we focus on H_2 gas because of its high degree of structure and our methodology hinges on the availability of additional proxies better suited to trace its structure. The impact of the other components of the γ-ray IE (specifically HI and dark gas [30]), and related uncertainties, is not considered in this study and will be the focus of later work. Since H_2 does not emit at a characteristic radio frequency, other molecules are used to trace its distribution. In particular, carbon monoxide (^{12}CO, or CO hereafter) is typically employed as a proxy. Radio surveys trace the distribution of CO across the sky and the H_2 column density is inferred by scaling the CO content by a conversion factor (X_{CO}) which gives the ratio of the integrated CO line emission to the H_2 column density. The bulk of the H_2 is traced following this methodology, and the survey of the CO $J = 1$–0 transition line from [31] has been widely employed. However, the CO line emission is typically optically thick in the denser cores of molecular clouds and it underestimates the total H_2 column density there. γ-ray IE models that employ CO to trace H_2 gas may therefore underestimate its finer structure. This limitation can be addressed by exploiting CO isotopologues, ^{13}CO and C^{18}O, also found in H_2 clouds. The line emission from these rarer isotopologues remains optically thin to larger column densities and therefore is more reliable to probe dense cores.

A. H_2 tracers

We employ the data from the Mopra Southern Galactic Plane CO Survey (data release 3) [32] to trace the denser H_2 regions. The survey covers a 50 square degree region, spanning Galactic longitudes $l = 300°$–$350°$ and latitudes $|b| \leq 0.5°$, and it targets the $J = 1 - 0$ transitions of CO, ^{13}CO, C^{18}O, and C^{17}O. Mopra is a 22 meter single dish radio telescope located $\sim$450 km from Sydney, Australia, targeting the 109–115 GHz $J = 1$–0 transitions of CO, ^{13}CO, C^{18}O, and C^{17}O. It utilizes a "Fast-On-The-Fly" mapping in 1 square degree segments, with each segment being comprised of orthogonal scans in longitudinal and latitudinal directions. Each square degree has an exposure of at least $\sim$20 hours. The data reduction process by the Mopra team, which involves six main stages of processing to perform the band-pass correction and background subtraction, yields data cubes of the brightness temperature for each spectral line, as a function of Galactic coordinates and local standard of rest velocity. The spectral resolution is 0.1 km sec^{-1}. To efficiently work with the Mopra observations we create a mosaic of the data over the full 50 square degree region for both CO and ^{13}CO. These maps are shown in Fig. 1, where the color scale gives the total line strength, W(CO), integrated over all velocities (-150 to 50 km s^{-1}). The vertical black lines show the footprint of the mosaic, i.e. regions where pixels from adjacent fields overlap. As can be seen, the emission shows discontinuities in these footprint regions. This is likely due to the fields having different noise levels resulting from the varying weather conditions of the observations. To avoid any potential complications with these regions they are masked
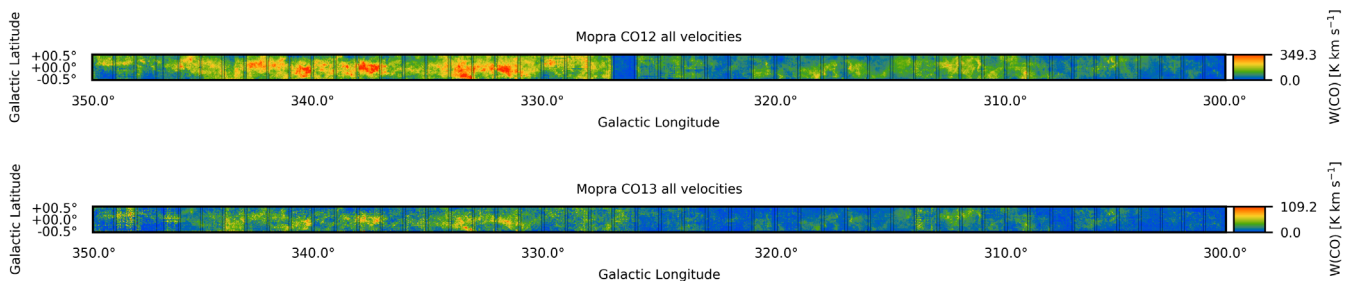

FIG. 1. Total line strength integrated over all velocities (-150 to 50 km s^{-1}) for CO (top) and ^{13}CO (bottom) from Mopra. The color scale is set to 2/3 of the maximum value, for illustration, and no smoothing is applied. The vertical black lines delimit the footprint of the mosaic, and the narrower region they enclose is masked in the analysis (see text).

in the analysis. Additionally, we slightly degrade the spatial resolution from 0.0083° to 0.03125°. This is done to speed up the computation time of the γ-ray intensity maps (see Sec. II C). We note that the CO maps customarily used to trace H_2 [31] have a spatial resolution of 0.25°, and thus the Mopra maps that we employ represent an 8× improvement. The emission shown in Fig. 1 also displays vertical and horizontal strips. This is a systematic feature due to the scanning method used in the observations, and it does not have any significant impact on our analysis.

To ensure the highest quality data in the rare isotopologues, only pixels for which the brightness temperature exceeds the 1σ noise provided by Mopra are used. Noise removal is necessary since the noise could otherwise predict spurious γ-ray emission (see Sec. II B for more details.) The noise threshold is chosen for consistency with the next stage of this work, where we train machine learning (ML) models on these data to predict ^{13}CO in regions of the sky where observations are not available. Because the optimization of ML models learns about the noise, our choice favors retaining more data for training purposes [33]. In this analysis we utilize the CO and ^{13}CO data, as the $C^{18}O$ emission is extremely sparse, and the $C^{17}O$ emission was too faint to be detected in the survey. For the region it surveys, the Mopra data provide a sharper view of the CO emission compared to [31], in addition to probing the rarer H_2 tracers.

B. H_2 column density

We calculate the H_2 column density corresponding to Mopra's CO and ^{13}CO, referred to as $N(H_2)_{CO}$ and $N(H_2)_{CO13}$, respectively. Following the method of [34], the gas is separated into 17 Galactocentric radial bins (or annuli) based on its velocity and therefore corresponding to different distances from the GC, assuming uniform circular motion about the GC (see Appendix A for details). The $N(H_2)_{CO}$ is determined as

$$N(H_2)_{CO} = W(CO) \times X_{CO}, \qquad (1)$$

where $W(CO)$ is the line strength of the CO gas, and we adopt the radially dependent X_{CO} from [34] for the 17 radial bins. An alternative assumption of a constant X_{CO} could also be considered when our methodology is applied to the data.

$N(H_2)_{CO13}$ is evaluated as

$$N(H_2)_{CO13} = N(CO13) \times \left[\frac{H_2}{CO13}\right]. \qquad (2)$$

where $N(CO13)$ is the ^{13}CO column density, and the abundance ratio $\left[\frac{H_2}{CO13}\right]$ is the conversion factor for the rarer species, ^{13}CO in this case. Following [32,35], we derive $N(CO13)$ assuming that the gas is in local thermodynamic equilibrium at a fixed excitation temperature of 10 K (the procedure is summarized in Appendix B). Since the conversion to column densities involves multiplying the line strength observed by Mopra by large factors, of order $\sim 10^{20}$, noise in regions with no gas emission would yield significant column density and, in turn, spurious predictions for the related γ-ray emission. This is especially problematic for our ultimate goal of comparing $N(H_2)_{CO12}$ to $N(H_2)_{CO13}$. To mitigate this issue we use the noise maps which have been provided by the Mopra team, as anticipated in Sec. II A. For each spatial pixel, the noise is determined from the standard deviation of the continuum channels for line-of-sight velocities containing no apparent signal. The observations were carried out over a wide variety of weather conditions, and this is reflected in the noise maps, which are not uniform over the Mopra region, but rather vary from field to field. In calculating the column density we only use pixels that are above the 1σ noise level. Otherwise, pixels that are below the 1σ noise level are masked. The abundance ratio $\left[\frac{H_2}{CO13}\right]$ is not tightly constrained. We choose the upper bound of the range $(2.7–7.5) \times 10^5$ provided in [36], in an attempt to assess the maximal impact on the γ-ray data, although it is not excluded that larger values are possible.

C. H_2-related γ-ray emission

The CR propagation code GALPROP (v56) [37–47] is used to evaluate the γ-ray intensity maps for the H_2-related emission traced by CO and ^{13}CO. GALPROP self-consistently calculates spectra and abundances of Galactic CR species and associated diffuse emissions (γ rays, but also radio, x rays) in 2D and 3D. We adopt the same GALPROP input parameters as described in [48]. GALPROP returns radially dependent γ-ray intensity all-sky maps (in the 17 Galactocentric annuli) which allow us to determine, for the region observed by Mopra, the additional contribution in γ
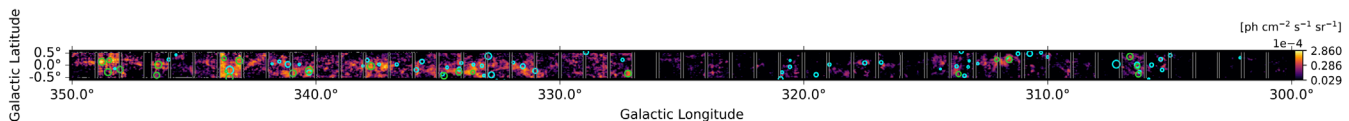

FIG. 2. The Modified Excess Template, calculated as the difference between the Modified Map and the baseline CO map. The color scale shows the γ-ray intensity. The solid cyan circles show unassociated γ-ray point sources in version 4FGL-DR2 of the fourth *Fermi*–LAT catalog [49], and the green circles show new sources that we find in this work (see text). The radius of each source corresponds to the 95% localization uncertainty.

rays from the H_2 traced by ^{13}CO, and assess its significance in simulated *Fermi*–LAT data. The difference between $N(H_2)_{CO13}$ and $N(H_2)_{CO}$ gives an estimate of the H_2 that is missed in dense regions when only CO is used as a tracer. To calculate the corresponding intensity in γ rays, we define the "Modified Map." This is calculated in the following way: for pixels with $N(H_2)_{CO13} > N(H_2)_{CO12}$, the value of $N(H_2)_{CO12}$ is replaced with the value of $N(H_2)_{CO13}$. We define the "Modified Excess Template" as the difference between the Modified Map and the baseline CO map, which accounts for the additional H_2-related γ-ray emission not included in current IE models, shown in Fig. 2.

III. SIGNIFICANCE OF THE γ-RAY EMISSION RELATED TO THE DISCRETE H_2 COMPONENT IN THE *Fermi*–LAT DATA

We evaluate the significance of the Modified Excess Template in the *Fermi*–LAT data by simulating the data collected between 2008 August 04 to 2020 November 11 ($\sim$12 years). The simulated events have energies in the range 1–100 GeV and are binned in eight energy bins per decade, for event class P8R3_CLEAN (FRONT + BACK). The analysis is performed using Fermipy (v0.19.0), which utilizes the Fermitools (v1.2.23). In these simulations, we only focus on the H_2-related γ-ray emission, and exclude all other components of the γ-ray sky. The goal is to assess the significance of the Modified Excess Template, i.e. the contribution of the newly modeled H_2 fine structure, in the optimistic scenario where all other components are satisfactorily modeled. The simulated events trace the H_2-related γ-ray emission modeled with the Modified Map. The simulated data are then fit based on a binned maximum likelihood method to a model that includes two components, the γ rays traced by the baseline CO map and the Modified Excess Template. The latter is assigned the spectrum determined by GALPROP (see Appendix C), and its normalization is free to vary in the fit. The normalization of the CO map is also free to vary and its spectrum constrained to that calculated by GALPROP. As mentioned above, the γ-ray flux is calculate in 17 radial bins, since the predicted H_2-related γ-ray emission depends on the CR density, which is a function of Galactocentric radius. In the simulations, the total emission is integrated along the line of sight. Moreover, the individual maps have a high level of degeneracy. We therefore combine the maps into four radial bins. Specifically, we combine bins 1–6, 7–10, 11–13, and 14–17, which we refer to as A1, A2, A3, and A4.

We simulate 1000 realizations of *Fermi*–LAT data, and calculate the test statistics (TS) for the nested models, $-2\log(L_0/L)$, where L_0 corresponds to value of the likelihood function for the null hypothesis (CO baseline), and L to the alternative hypothesis (CO baseline and Modified Excess Template). The statistical significance is approximated by $\sigma \approx \sqrt{TS}$. The distribution of the $\sqrt{TS}$ for the 1000 simulations is shown in Fig. 3. The mean of the
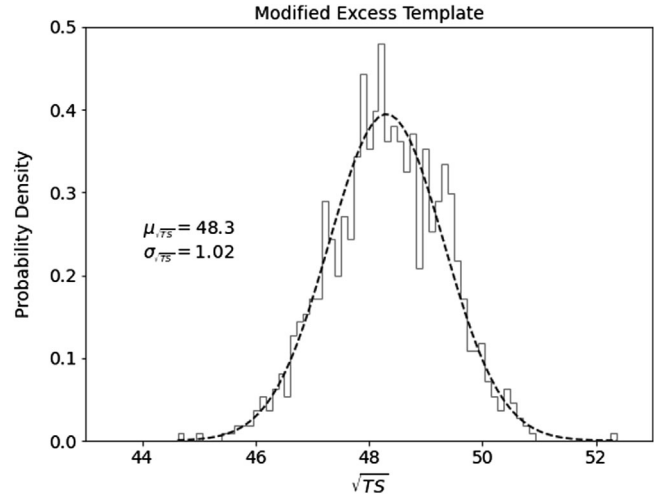

FIG. 3. Distribution of the statistical significance ($\sigma \approx \sqrt{TS}$) of the Modified Excess Template for the $50° \times 1°$ region covered by Mopra for 1000 realizations of $\sim$12 years of *Fermi*–LAT data. A fit with a Gaussian function is overlaid.

distribution is 48.30 ± 1.02, for the 50 squared degree Mopra region, and therefore very significant in a scenario where other components contributing to the *Fermi*–LAT data are perfectly modeled, and if the γ-ray emission traced by ^{13}CO is at the high end of the range we have considered (with the caveats discussed above).

The fractional residuals as a function of energy for the 1000 simulations are shown in Fig. 4. They are consistent with zero, as expected. Figure 5 shows the distributions of the flux of each model component, including the Modified Excess Template. In the Mopra region, the mean integrated flux for this component is $(8.3 \pm 0.2) \times 10^{-8}$ ph cm^{-2} s^{-1}.
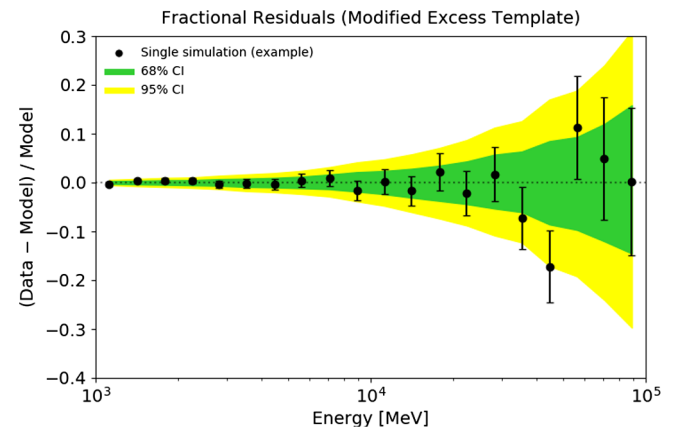

FIG. 4. Fractional count residuals as a function of energy. The green and yellow bands show the 68% and 95% confidence regions from 1000 simulations, respectively. As an example, we also plot the results for a single simulation, shown with black data points.
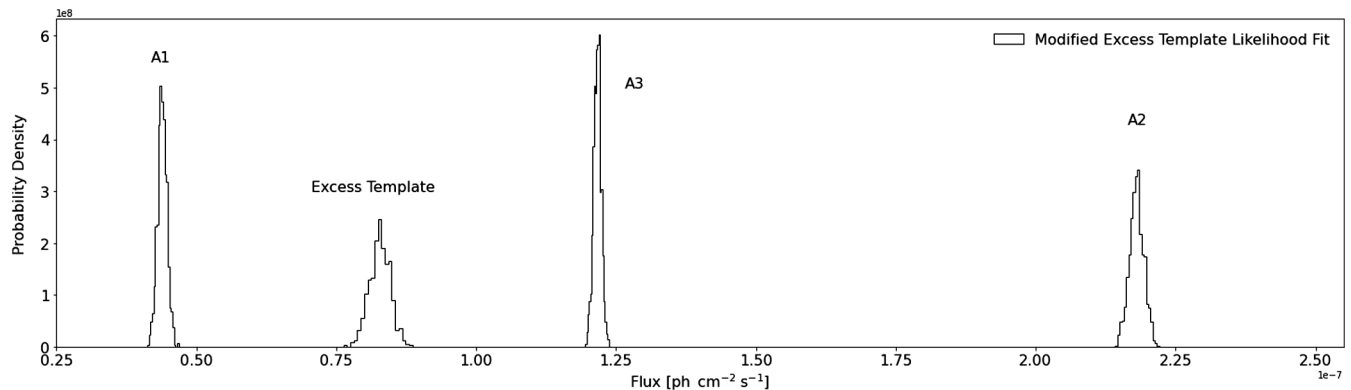
FIG. 5. The distributions of fluxes for each component of the best-fit model using the Modified Excess Template over the full region for 1000 realizations of ~ 12 years of *Fermi*–LAT data. Note that one of the annuli (A4) has negligible contribution and the normalization was fixed in the fitting process (corresponding to a flux of 4.98×10^{-9} $\mathrm{ph\,cm^{-2}\,s^{-1}}$).

IV. IMPLICATIONS FOR THE GALACTIC CENTER EXCESS

Overall, the Modified Excess Template accounts for a fair fraction (21%) of the total H_2-related γ-ray emission in the Mopra region. For comparison, the integrated GC excess flux in a $15° \times 15°$ region around the GC (the full region is considered), which is $4\times$ larger than the region observed by Mopra, is in the range $18.3 - 25.0 \times 10^{-8}$ $\mathrm{ph\,cm^{-2}\,s^{-1}}$ (from [2]). In intensities, the GC excess corresponds to $2.67 - 3.65 \times 10^{-6}$ $\mathrm{ph\,cm^{-2}\,s^{-1}\,sr^{-1}}$ compared to 5.43×10^{-6} $\mathrm{ph\,cm^{-2}\,s^{-1}\,sr^{-1}}$ for the Modified Excess Template. Because of the different spatial morphology of the GC excess and H_2-related γ-ray emission traced by ^{13}CO, a direct comparison is unwarranted and we do not expect the latter to account for the majority of the GC excess. However, the H_2 emission extends beyond the latitudes considered in this study and, albeit dimmer at higher latitudes, the estimates provided here do not indicate its small scale component to be negligible. We estimate this contribution in the GC region by considering, as above, a $15° \times 15°$ region around the GC. In this region, the contribution from H_2-related emission (pi0 decay only) traced by CO is $\sim 55 \times 10^{-8}$ $\mathrm{ph\,cm^{-2}}$ [2]. If we adopt the same fraction of unmodeled pointlike emission for H_2 as we find in the Mopra region, i.e. approximately 21%, this fraction translates into a very rough estimate of this pointlike contribution in the same region of the GC excess, i.e. about 11.5×10^{-8} $\mathrm{ph\,cm^{-2}}$, or 46%–63% of the GC excess for the same region. This estimate shows that the pointlike emission could correspond to a significant fraction of the GC excess.

This contribution could therefore confuse the GC excess morphology, depending on the exact H_2 emission outside of $\pm 0.5°$ in latitude, because the techniques that track the pointlike fluctuations could erroneously ascribe unaccounted pointlike emission (originating from H_2 gas in this case) to the GC excess [21]. Considerations based on

the spectrum of the unresolved source population could be powerful to settle this degeneracy, however a robust determination is required.

V. IMPLICATIONS FOR POINT SOURCE DETECTION

We identify the structure traced by ^{13}CO that is bright enough to be detected as a *Fermi*–LAT point source and compare it to the unassociated sources in version 4FGL-DR2 of the fourth *Fermi*–LAT catalog of γ-ray sources [49]. A significant overlap would indicate that its brightest contribution has already been detected by *Fermi*–LAT and validate the methodology to trace this component. To this end, we perform a likelihood fit where, instead of including the Modified Excess Template in the model, we only consider the baseline CO map and find additional point sources using the fermipy *find_srcs* function. The method calculates TS maps, and identifies point sources based on peaks in the TS. We use a test point source modeled with a power law spectrum with spectral index $= 2$, and a minimum TS threshold of $TS \geq 16$. An index of 2.7 is compatible with CRs interacting with gas, and if used, it yields consistent results. In total we find 23 new point sources with $TS \geq 16$, which are shown with green circles in Fig. 2. For comparison, we also overlay 4FGL-DR2 unassociated sources. We find that 8/23 (35%) of the new sources are spatially consistent with an unassociated 4FGL-DR2 source (based on an overlap of the 95% localization errors), which accounts for 8/46 (17%) of the total unassociated sources in the region. To quantify the probability that the associations happen by chance, we perform 1000 simulations, where for each realization we randomly distribute 23 sources in the Mopra region. For each source the Galactic coordinates are drawn from a uniform distribution and we assign an error radius drawn from a Gaussian distribution, with the mean and standard deviation determined from the 23 detected sources. From

the 1000 simulations we find the average number of random associations to be 3.16 ± 1.72, which corresponds to a p-value [i.e. $N(\geq 8)/1000$] of 0.012. It is therefore likely that the brightest of the pointlike emission traced by Mopra ^{13}CO have already been detected in the *Fermi*–LAT data.

VI. DISCUSSION

The results presented here demonstrate that there likely exists significant structure in the H_2-related γ-ray emission detected by *Fermi*–LAT which is not currently included in the IE models. Since its spatial morphology has pointlike features, it directly affects the detection of resolved and, potentially, unresolved point source populations in the γ-ray data. More specifically, we have discussed the impact on the 4FGL-DR2 catalog and on the interpretation of the GC excess. Although in this analysis we have focused on the region covered by Mopra, similar conclusions would hold elsewhere because of the same limitations in tracing H_2. The methodology described here however can only be readily applied to limited regions of the sky because of the paucity of observations of the rare H_2 tracers. Unfortunately, we cannot simply extrapolate the Modified Excess Template to other regions, even with a less ambitious goal of providing only an estimate of this emission. This is because the Mopra data on which it is based is tightly confined, especially in latitude. To address the limited available observations, we have resorted to ML to develop a methodology that predicts the distribution of the small scale H_2-related γ-ray emission for other regions of the sky based on the existing Mopra data. Because of its complexity, we describe the ML related work in a companion paper [33], where we show that we can train a convolutional neural network to predict ^{13}CO based on CO Mopra observations, and reproduce the H_2-related small scale structure traced by ^{13}CO within the statistical uncertainty of the *Fermi*–LAT data in the Mopra region. We conclude that our results justify applying this methodology to other regions of the sky by extending it to employ the all-sky CO survey [31].

VII. SUMMARY AND CONCLUSIONS

In this paper, we assess whether there is pointlike emission in the γ-ray data associated with the interstellar gas and not currently included in models of the Galactic interstellar γ-ray emission. We argue that this emission could significantly impact the detection of γ-ray point sources along the Galactic plane, and hinder the characterization of extended γ-ray sources, such as the GC excess. We employ the data from the Mopra Southern Galactic Plane CO Survey, which includes tracers of the small scale structure of the H_2-related γ rays, to improve models by more accurately describing the pointlike features in the gas. We find that significant pointlike emission originates from H_2 gas and the significance could be as high

as $\sqrt{TS} \sim 48$ (depending on assumptions) in a $50° \times 1°$ region covered by Mopra, corresponding to $\sim21\%$ of the modeled H_2-related γ-ray emission in the region. We also show that this newly found pointlike component may account for some fraction ($\lesssim17\%$) of γ-ray point sources detected by *Fermi*–LAT in the Galactic plane whose origin is so far unknown. That a significant number of unidentified 4FGL-DR2 sources along the Galactic plane originate from unmodeled structure in the gas is not unexpected, but here we develop a robust and reliable methodology to identify the contribution of both bright and dimmer components of the H_2 gas discrete emission. We emphasize that our results depend on the assumptions we have adopted, e.g. a less conservative ^{13}CO abundance ratio. Because of the significance of this emission under plausible assumptions, we conclude that its contribution in the GC region could introduce a significant systematic uncertainty in determining whether the GC excess is smooth or pointlike, and therefore more consistent with a dark matter or pulsar interpretation, specifically when relying on statistical techniques such as the NPTF. Identifying this component in the GC region could be a crucial step to settle the origin of the GC excess.

APPENDIX A: SEPARATING THE GAS INTO GALACTOCENTRIC ANNULI

The H_2 gas is placed at Galactocentric radii based on its velocity, assuming uniform circular motion around the Galactic center (GC), described with the rotation curve $V(R)$. The velocity with respect to the local standard of rest (V_{LSR}) of a region with Galactocentric distance R, viewed toward Galactic coordinates l, b is given by [34]

$$V_{LSR} = \left(\frac{R_\odot}{R} V(R) - V_\odot \right) \sin(l) \cos(b). \quad (A1)$$

We use the parametrized rotation curve of [50], with $R_\odot = 8.5$ kpc for the distance from the GC to the Sun, and $V_\odot = 220$ km s^{-1} for the velocity of the Sun around the GC (e.g. see [34] and references therein). Since the Mopra data is within $0.5°$ from the Galactic plane, we use the small angle approximation $\cos(b) \approx 1$. Following the same procedure as [34], we bin the gas in 17 discrete radial bins, as

TABLE I. Radial bins.

Bin	$R_{\min}$ [kpc]	$R_{\max}$ [kpc]	$X_{CO}(\times 10^{-20})$ [cm^{-2} (K km s^{-1})$^{-1}$]
1	0	1.5	0.36
2	1.5	2.0	1.01
3	2.0	2.5	1.04
4	2.5	3.0	1.06
5	3.0	3.5	1.11
6	3.5	4.0	1.09
7	4.0	4.5	1.15
8	4.5	5.0	1.19
9	5.0	5.5	1.2
10	5.5	6.5	1.22
11	6.5	7.0	1.33
12	7.0	8.0	1.4
13	8.0	10.0	0.72
14	10.0	11.5	7.0
15	11.5	16.5	24.55
16	16.5	19.0	131.79
17	19.0	50.0	532.47

summarized in Table I. Figure 6 shows the local standard of rest velocity as a function of Galactocentric radius, calculated for longitudes between 300°–350°. We have verified that the resulting gas distributions for the radial bins are in good agreement with those from [2,48], which use the same radial binning with the CO maps from [31].
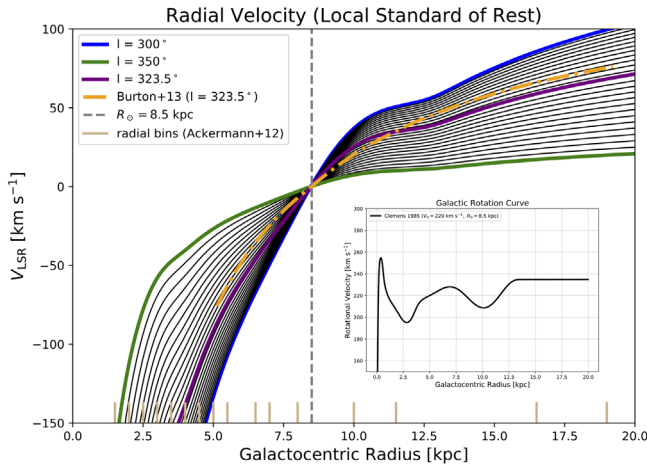

FIG. 6. Local standard of rest velocity (V_{LSR}) as a function of Galactocentric radius, calculated for Galactic longitudes between 300°–350°. The calculations are made assuming uniform circular rotation described by the Galactic rotation curve of [50], shown in the inset. The Solar radius is assumed to be 8.5 kpc, indicated with the dashed gray line. The purple curve is calculated at a longitude of 323.5°, which is compared to the result from [51], shown with a dash-dotted orange curve (note, however, that they use a different Galactic rotation curve, which leads to slight differences in V_{LSR}). The 17 radial bins used in the analysis are shown with the tan bins along the x axis.

APPENDIX B: CALCULATING THE H$_2$ COLUMN DENSITY

We employ the Mopra data to calculate the corresponding H$_2$ column density separately for both CO and ^{13}CO, which we label as $N(H_2)_{CO12}$ and $N(H_2)_{CO13}$, respectively. We note that in both cases we correct for the beam efficiency using a value of 1/0.55 [32]. To calculate $N(H_2)_{CO12}$ we use

$$N(H_2)_{CO12} = W(CO) \times X_{CO}, \qquad (B1)$$

where we employ a radially dependent conversion factor (X_{CO}) for the 17 radial bins, as determined in [34], based on a maximum likelihood fit to the γ-ray data. The values are given in the last column of Table I.

In general, $N(H_2)_{CO13}$ can be calculated from the ^{13}CO column density, $N(CO13)$, and the abundance ratio, $[\frac{H_2}{CO13}]$:

$$N(H_2)_{CO13} = N(CO13) \times \left[\frac{H_2}{CO13}\right]. \qquad (B2)$$

We follow the procedure from [32,35], which we summarize below. We derive $N(CO13)$ assuming that the gas is in local thermodynamic equilibrium at a fixed excitation temperature of 10 K:

$$N(CO13) = \frac{3.0 \times 10^{14}}{1 - e^{-5.3/T}} \times T \int \tau^{13}(\nu)d\nu, \qquad (B3)$$

where τ^{13} is the ^{13}CO optical depth and 5.3 K is the energy level of the $J = 1 - 0$ transition. T is the line excitation temperature (assumed to be the same as the kinetic temperature of the gas) and here we use T = 10 K. The optical depth is calculated as

$$\tau^{13} = -\ln\left[1 - \frac{T_B^{13}}{5.3}\left\{\left[\exp\left(\frac{5.3}{T}\right) - 1\right]^{-1} - 0.16\right\}^{-1}\right],$$

where T_B^{13} is the line intensity measured by Mopra as a function of velocity.

To approximate a physically viable range for the abundance ratio we use the range of values from [36], based on a study of the Perseus Molecular Cloud Complex. Specifically, we estimate that

$$\left[\frac{H_2}{CO13}\right] \sim (2.7–7.5) \times 10^5. \qquad (B4)$$

APPENDIX C: PREDICTED γ-RAY FLUX AND SPECTRUM FOR THE H$_2$ TRACED BY MOPRA

The CR propagation code GALPROP (v56) calculates the γ-ray sky maps for the H$_2$-related emission. Here, we employ the GALPROP input parameters described in [48] to
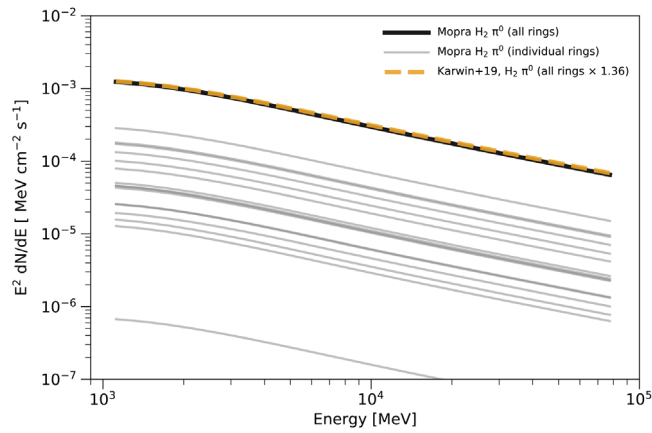
FIG. 7. γ-ray spectra for the H_2-related components summed over the Mopra region. The gray curves are for the individual radial bins, and the black curve is the total model. The dashed yellow curve is the total spectrum from [48], scaled by a factor of 1.36, which is the systematic offset of the Mopra data compared to the CO maps in [31].

determine the γ-ray emission related to the H_2 column density $N(H_2)_{CO12}$ traced by Mopra in the 17 radial bins.

Figure 7 shows the γ-ray spectra corresponding to the input column density $N(H_2)_{CO12}$, summed over the entire sky. As a consistency check, we compare it to the spectra from [48], based on the CO maps from [31]. The Mopra data was found to be systematically higher than the CO observations in [31] by a factor of 1.36 (as discussed in [32]), so we include this scaling factor in the comparison. As can be seen, the two spectra are in excellent agreement.

---

[1] S. Abdollahi *et al.*, Fermi large area telescope fourth source catalog, Astrophys. J. Suppl. Ser. **247,** 33 (2020).

[2] M. Ajello, A. Albert, W. Atwood, G. Barbiellini, D. Bastieri, K. Bechtol, R. Bellazzini, E. Bissaldi, R. Blandford, E. Bloom *et al.*, Fermi-LAT observations of high-energy γ-ray emission toward the Galactic center, Astrophys. J. **819,** 44 (2016).

[3] S. Abdollahi *et al.*, Incremental Fermi large area telescope fourth source catalog, Astrophys. J. Suppl. Ser. **260,** 53 (2022).

[4] L. Goodenough and D. Hooper, Possible evidence for dark matter annihilation in the inner Milky Way from the Fermi Gamma Ray Space Telescope, arXiv:0910.2998.

[5] D. Hooper and L. Goodenough, Dark matter annihilation in the Galactic center as seen by the Fermi gamma ray space telescope, Phys. Lett. B **697,** 412 (2011).

[6] D. Hooper and T. Linden, Origin of the gamma rays from the Galactic center, Phys. Rev. D **84,** 123005 (2011).

[7] K. N. Abazajian, The consistency of Fermi-LAT observations of the Galactic center with a millisecond pulsar population in the central stellar cluster, J. Cosmol. Astropart. Phys. 03 (2011) 010.

[8] K. N. Abazajian and M. Kaplinghat, Detection of a gamma-ray source in the Galactic center consistent with extended emission from dark matter annihilation and concentrated astrophysical emission, Phys. Rev. D **86,** 083511 (2012).

[9] D. Hooper and T. R. Slatyer, Two emission mechanisms in the Fermi bubbles: A possible signal of annihilating dark matter, Phys. Dark Universe **2,** 118 (2013).

[10] C. Gordon and O. Macías, Dark matter and pulsar model constraints from Galactic center Fermi-LAT gamma-ray observations, Phys. Rev. D **88,** 083521 (2013).

[11] K. Abazajian, N. Canac, S. Horiuchi, and M. Kaplinghat, Astrophysical and dark matter interpretations of extended gamma ray emission from the Galactic center, Phys. Rev. D **90** (2014).

[12] T. Daylan, D. P. Finkbeiner, D. Hooper, T. Linden, S. K. Portillo, N. L. Rodd, and T. R. Slatyer, The characterization of the gamma-ray signal from the central Milky Way: A case for annihilating dark matter, Phys. Dark Universe **12,** 1 (2016).

[13] F. Calore, I. Cholis, and C. Weniger, Background model systematics for the Fermi GeV excess, J. Cosmol. Astropart. Phys. 03 (2015) 038.

[14] O. Macias, C. Gordon, R. M. Crocker, B. Coleman, D. Paterson, S. Horiuchi, and M. Pohl, Galactic bulge preferred over dark matter for the Galactic center gamma-ray excess, Nat. Astron. **2,** 387 (2018).

[15] O. Macias, S. Horiuchi, M. Kaplinghat, C. Gordon, R. M. Crocker, and D. M. Nataf, Strong evidence that the galactic bulge is shining in gamma rays, J. Cosmol. Astropart. Phys. 09 (2019) 042.

[16] R. Bartels, E. Storm, C. Weniger, and F. Calore, The Fermi-LAT GeV excess as a tracer of stellar mass in the galactic bulge, Nat. Astron. **2,** 819 (2018).

[17] M. Pohl, O. Macias, P. Coleman, and C. Gordon, Assessing the impact of hydrogen absorption on the characteristics of the Galactic center excess, Astrophys. J. **929,** 136 (2022).

[18] S. Murgia, The Fermi-LAT Galactic center excess: Evidence of annihilating dark matter?, Annu. Rev. Nucl. Part. Sci. **70,** 455 (2020).

[19] R. Bartels, S. Krishnamurthy, and C. Weniger, Strong Support for the Millisecond Pulsar Origin of the Galactic Center GeV Excess, Phys. Rev. Lett. **116,** 051102 (2016).

[20] S. K. Lee, M. Lisanti, B. R. Safdi, T. R. Slatyer, and W. Xue, Evidence for Unresolved γ-Ray Point Sources in the Inner Galaxy, Phys. Rev. Lett. **116,** 051103 (2016).

[21] R. K. Leane and T. R. Slatyer, Revival of the Dark Matter Hypothesis for the Galactic Center Gamma-Ray Excess, Phys. Rev. Lett. **123,** 241101 (2019).

[22] Y.-M. Zhong, S. D. McDermott, I. Cholis, and P. J. Fox, Testing the Sensitivity of the Galactic Center Excess to the Point Source Mask, Phys. Rev. Lett. **124,** 231103 (2020).

[23] R. K. Leane and T. R. Slatyer, Spurious Point Source Signals in the Galactic Center Excess, Phys. Rev. Lett. **125,** 121105 (2020).

[24] R. K. Leane and T. R. Slatyer, The enigmatic Galactic center excess: Spurious point sources and signal mismodeling, Phys. Rev. D **102,** 063019 (2020).

[25] M. Buschmann, N. L. Rodd, B. R. Safdi, L. J. Chang, S. Mishra-Sharma, M. Lisanti, and O. Macias, Foreground mismodeling and the point source explanation of the Fermi Galactic center excess, Phys. Rev. D **102,** 023023 (2020).

[26] F. Calore, F. Donato, and S. Manconi, Dissecting the Inner Galaxy with γ-Ray Pixel Count Statistics, Phys. Rev. Lett. **127,** 161102 (2021).

[27] F. List, N. L. Rodd, and G. F. Lewis, Extracting the Galactic center excess' source-count distribution with neural nets, Phys. Rev. D **104,** 123022 (2021).

[28] S. Mishra-Sharma and K. Cranmer, Neural simulation-based inference approach for characterizing the Galactic center γ-ray excess, Phys. Rev. D **105,** 063017 (2022).

[29] B. Balaji, I. Cholis, P. J. Fox, and S. D. McDermott, Analyzing the gamma-ray sky with wavelets, Phys. Rev. D **98,** 043009 (2018).

[30] I. A. Grenier, J.-M. Casandjian, and R. Terrier, Unveiling extensive clouds of dark gas in the solar neighborhood, Science **307,** 1292 (2005).

[31] T. M. Dame, D. Hartmann, and P. Thaddeus, The milky way in molecular clouds: A new complete CO survey, Astrophys. J. **547,** 792 (2001).

[32] C. Braiding, G. F. Wong, N. I. Maxted, D. Romano, M. G. Burton, R. Blackwell, M. D. Filipović, M. S. R. Freeman, B. Indermuehle, J. Lau *et al.*, The Mopra Southern Galactic Plane CO survey—Data release 3, Pub. Astron. Soc. Aust. **35,** e029 (2018).

[33] A. Shmakov, M. Tavakoli, P. Baldi, C. M. Karwin, A. Broughton, and S. Murgia, Deep learning models of the discrete component of the Galactic interstellar γ-ray emission, Phys. Rev. D **107,** 063018 (2023).

[34] M. Ackermann, M. Ajello, W. Atwood, L. Baldini, J. Ballet, G. Barbiellini, D. Bastieri, K. Bechtol, R. Bellazzini, B. Berenji *et al.*, Fermi-LAT observations of the diffuse γ-ray emission: Implications for cosmic rays and the interstellar medium, Astrophys. J. **750,** 3 (2012).

[35] T. L. Wilson, K. Rohlfs, and S. Hüttemeister, *Tools of Radio Astronomy*, Astronomy and Astrophysics Library (Springer-Verlag, Berlin, Heidelberg, 2009).

[36] J. E. Pineda, P. Caselli, and A. A. Goodman, CO isotopologues in the Perseus Molecular Cloud Complex: The X-factor and regional variations, Astrophys. J. **679,** 481 (2008).

[37] I. V. Moskalenko and A. W. Strong, Production and propagation of cosmic ray positrons and electrons, Astrophys. J. **493,** 694 (1998).

[38] I. V. Moskalenko and A. W. Strong, Anisotropic inverse Compton scattering in the galaxy, Astrophys. J. **528,** 357 (2000).

[39] A. W. Strong and I. V. Moskalenko, Propagation of cosmic-ray nucleons in the galaxy, Astrophys. J. **509,** 212 (1998).

[40] A. W. Strong, I. V. Moskalenko, and O. Reimer, Diffuse continuum gamma-rays from the galaxy, Astrophys. J. **537,** 763 (2000); Astrophys. J. **541,** 1109(E) (2000).

[41] V. S. Ptuskin, I. V. Moskalenko, F. C. Jones, A. W. Strong, and V. N. Zirakashvili, Dissipation of magnetohydrodynamic waves on energetic particles: Impact on interstellar turbulence and cosmic-ray transport, Astrophys. J. **642,** 902 (2006).

[42] A. W. Strong, I. V. Moskalenko, and V. S. Ptuskin, Cosmic-ray propagation and interactions in the Galaxy, Annu. Rev. Nucl. Phys. Sci. **57,** 285 (2007).

[43] A. E. Vladimirov, S. W. Digel, G. Johannesson, P. F. Michelson, I. V. Moskalenko, P. L. Nolan, E. Orlando, T. A. Porter, and A. W. Strong, GALPROP WebRun: An internet-based service for calculating galactic cosmic ray propagation and associated photon emissions, Comput. Phys. Commun. **182,** 1156 (2011).

[44] G. Jóhannesson *et al.*, Bayesian analysis of cosmic-ray propagation: Evidence against homogeneous diffusion, Astrophys. J. **824,** 16 (2016).

[45] T. A. Porter, G. Johannesson, and I. V. Moskalenko, High-energy gamma rays from the Milky Way: Three-dimensional spatial models for the cosmic-ray and radiation field densities in the interstellar medium, Astrophys. J. **846,** 67 (2017).

[46] G. Johannesson, T. A. Porter, and I. V. Moskalenko, The three-dimensional spatial distribution of interstellar gas in the Milky Way: Implications for cosmic rays and high-energy gamma-ray emissions, Astrophys. J. **856,** 45 (2018).

[47] Y. Génolini, D. Maurin, I. V. Moskalenko, and M. Unger, Current status and desired precision of the isotopic production cross sections relevant to astrophysics of cosmic rays: Li, Be, B, C, and N, Phys. Rev. C **98,** 034611 (2018).

[48] C. M. Karwin, S. Murgia, S. Campbell, and I. V. Moskalenko, Fermi-LAT observations of γ-ray emission toward the outer halo of M31, Astrophys. J. **880,** 95 (2019).

[49] J. Ballet, T. H. Burnett, S. W. Digel, and B. Lott, Fermi large area telescope fourth source catalog data release 2, Astrophys. J. Suppl. Ser. **247,** 33 (2020).

[50] D. P. Clemens, Massachusetts-Stony Brook Galactic plane CO survey: The galactic disk rotation curve, Astrophys. J. **295,** 422 (1985).

[51] M. G. Burton, C. Braiding, C. Glueck, P. Goldsmith, J. Hawkes, D. J. Hollenbach, C. Kulesa, C. L. Martin, J. L. Pineda, G. Rowell *et al.*, The Mopra Southern Galactic Plane CO survey, Pub. Astron. Soc. Aust. **30,** E044 (2013).